US 20190003064A1

(19) **United States**

(12) **Patent Application Publication**

Chou et al.

(10) **Pub. No.: US 2019/0003064 A1**

(43) **Pub. Date: Jan. 3, 2019**

(54) **CRUMPLED TRANSITION METAL DICHALCOGENIDE SHEETS**

(71) Applicants: **Vincent Tung**, (US); **Yen-Chang Chen**, (US); **National Technology & Engineering Solutions of Sandia, LLC**, Albuquerque, NM (US)

(72) Inventors: **Stanley Shihyao Chou**, Albuquerque, NM (US); **Vincent Tung**, Emeryville, CA (US); **Yen-Chang Chen**, San Jose, CA (US)

(21) Appl. No.: **16/010,650**

(22) Filed: **Jun. 18, 2018**

Related U.S. Application Data

(60) Provisional application No. 62/526,828, filed on Jun. 29, 2017.

Publication Classification

(51) **Int. Cl.**

C25B 11/04	(2006.01)
C25B 1/04	(2006.01)

(52) **U.S. Cl.**

CPC ***C25B 11/0447*** (2013.01); ***C25B 11/0415*** (2013.01); ***C25B 11/0405*** (2013.01); ***C25B 1/04*** (2013.01)

(57) **ABSTRACT**

An electrohydrodynamic (EHD) method results in charge driven droplet fission and volumetric shrinkage of metal dichalcogenide sheet droplets, thus wrinkling individual exfoliated metal dichalcogenide sheets on the nanoscale. For example, the method can be used to activate the basal plane of solution exfoliated, stable 2H reverted sheets of MoS_2. In this manner, the basal plane of 2H MoS_2 can be strained at an unprecedented scale (3.7%), resulting in charge transport to basal plane defects. The resulting crumpled MoS_2 integrates few layer sheets and atomistic defects with nano- and micro-scale ridges and vertices to enable centimeter-length films that elevate the catalytic site count of MoS_2 from 1.0×10^{14} sites/cm^2 to 2.93×10^{17} sites/cm^2 (planar 2H vs. crumpled 2H) and a turn-over-frequency (TOF) from 0.016 s^{-1} to 0.130 s^{-1}.

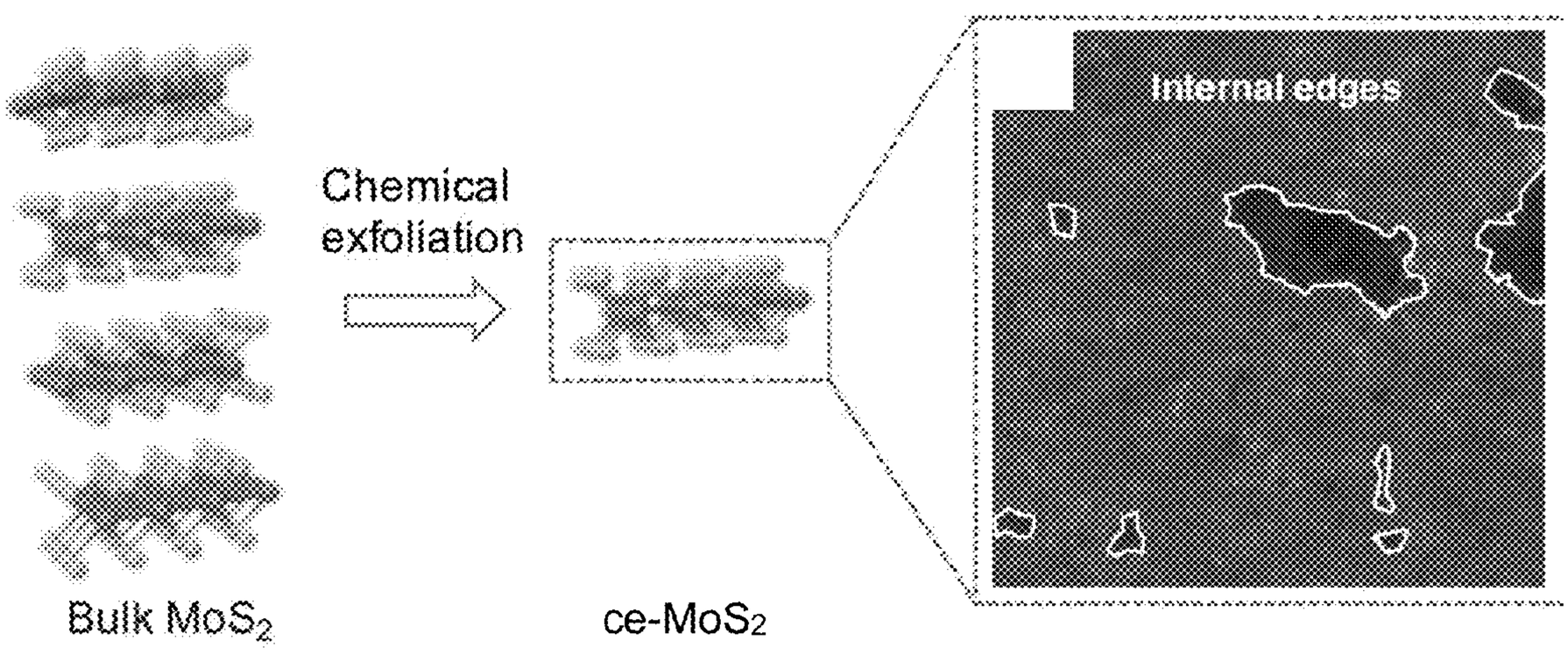

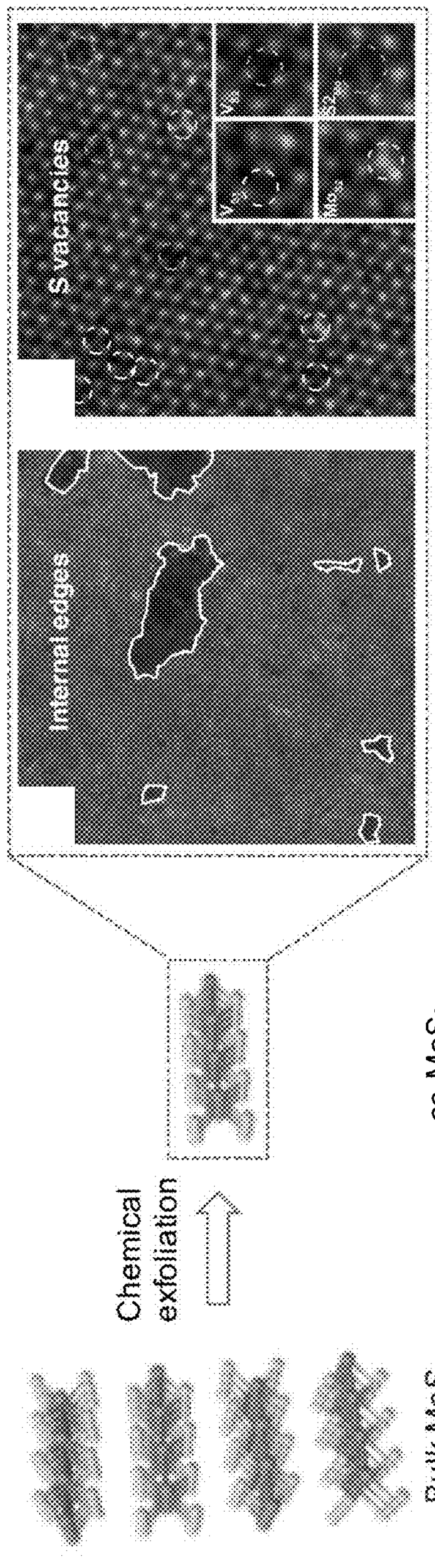

FIG. 1(c)

FIG. 1(b)

FIG. 1(a)

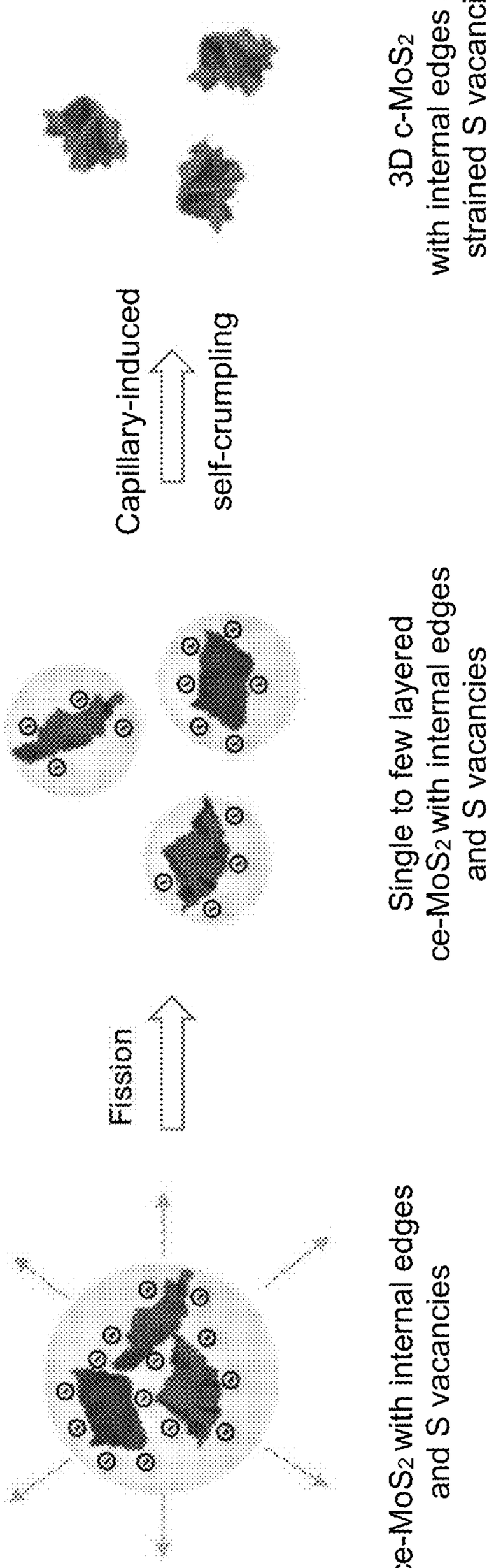
ce-MoS2 with internal edges and S vacancies
Fission
Single to few layered ce-MoS2 with internal edges and S vacancies
Capillary-induced self-crumpling
3D c-MoS2 with internal edges and strained S vacancies

FIG. 2

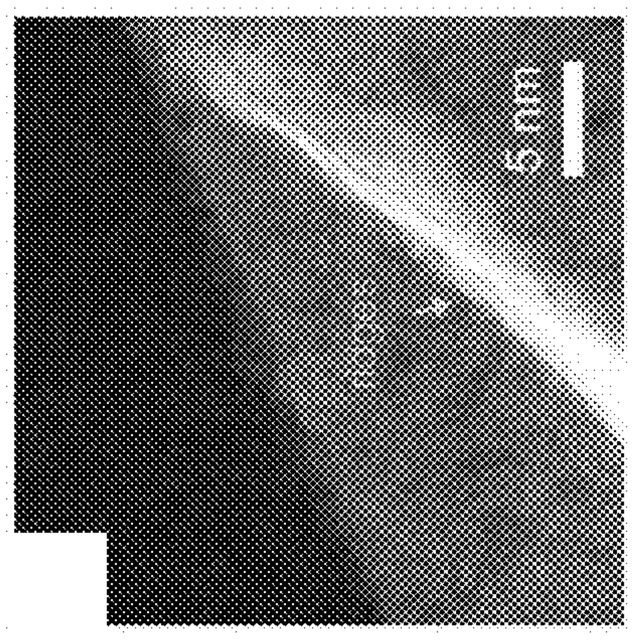

FIG. 3(d)

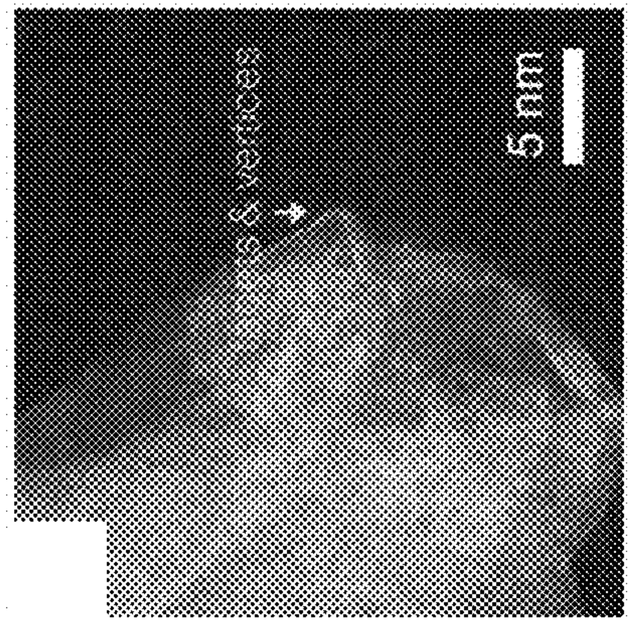

FIG. 3(c)

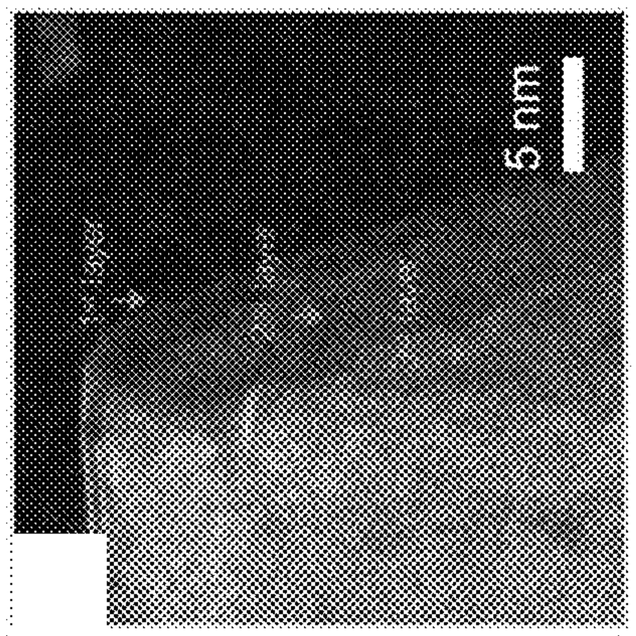

FIG. 3(b)

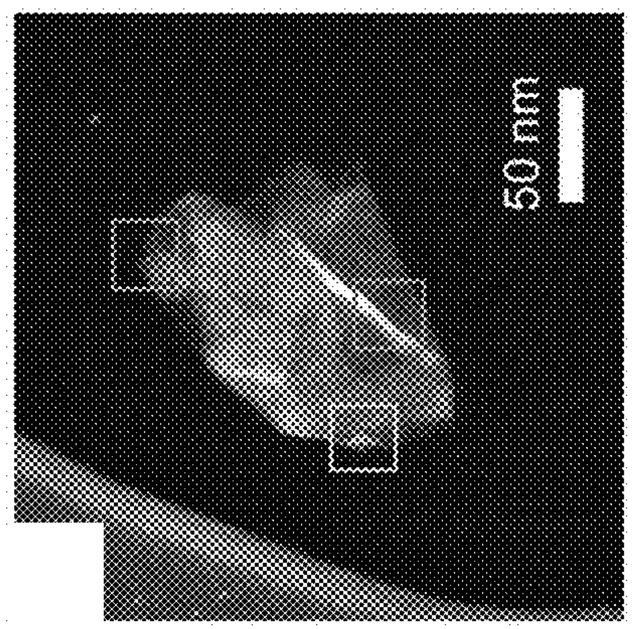

FIG. 3(a)

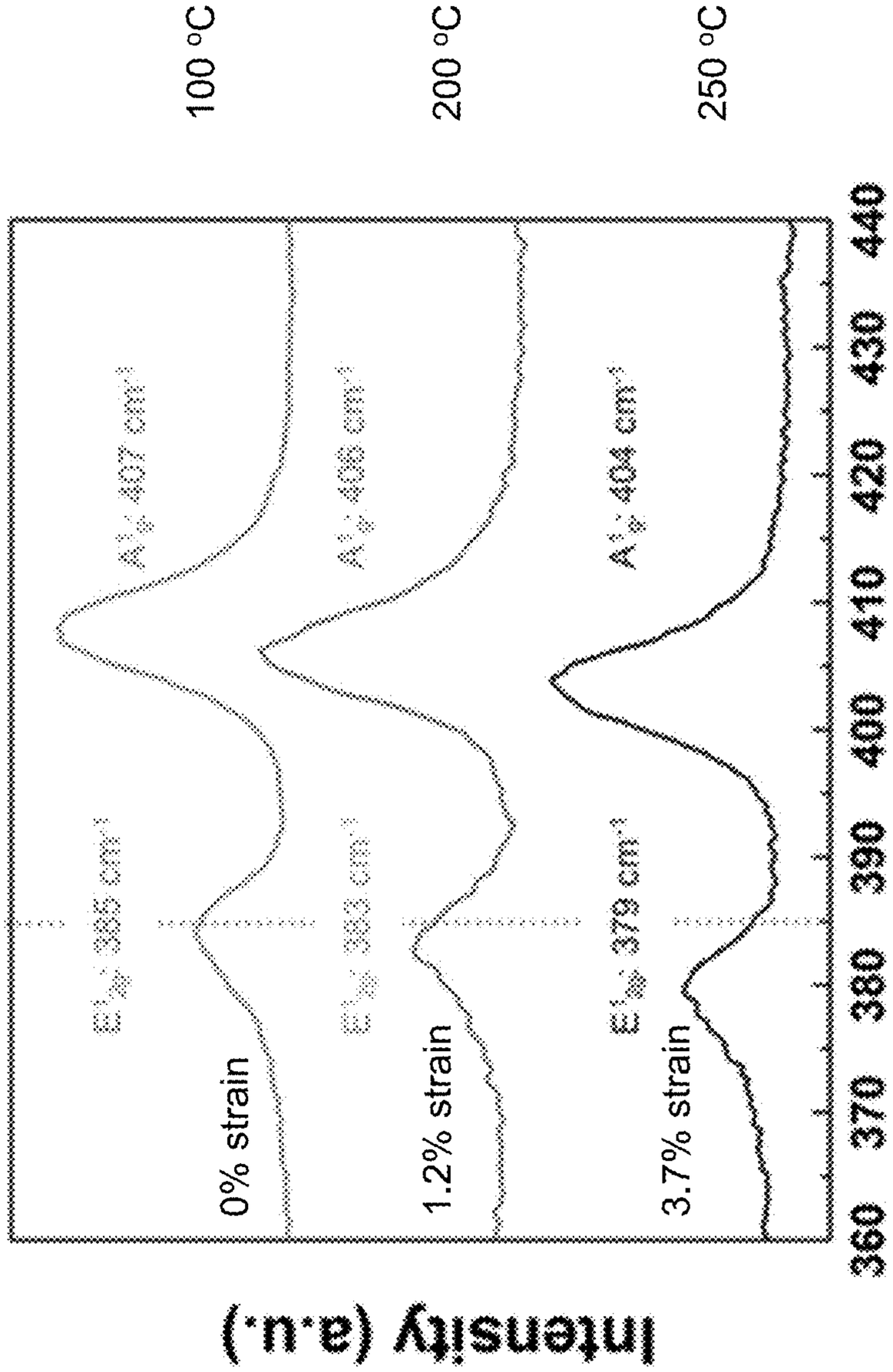
100 °C
200 °C
250 °C
E^1_{2g}: 385 cm^{-1}
A^1_g: 407 cm^{-1}
E^1_{2g}: 383 cm^{-1}
A^1_g: 408 cm^{-1}
E^1_{2g}: 379 cm^{-1}
A^1_g: 404 cm^{-1}
0% strain
1.2% strain
3.7% strain
360
370
380
390
400
410
420
430
440
Raman shift (cm^{-1})
Intensity (a.u.)

FIG. 4

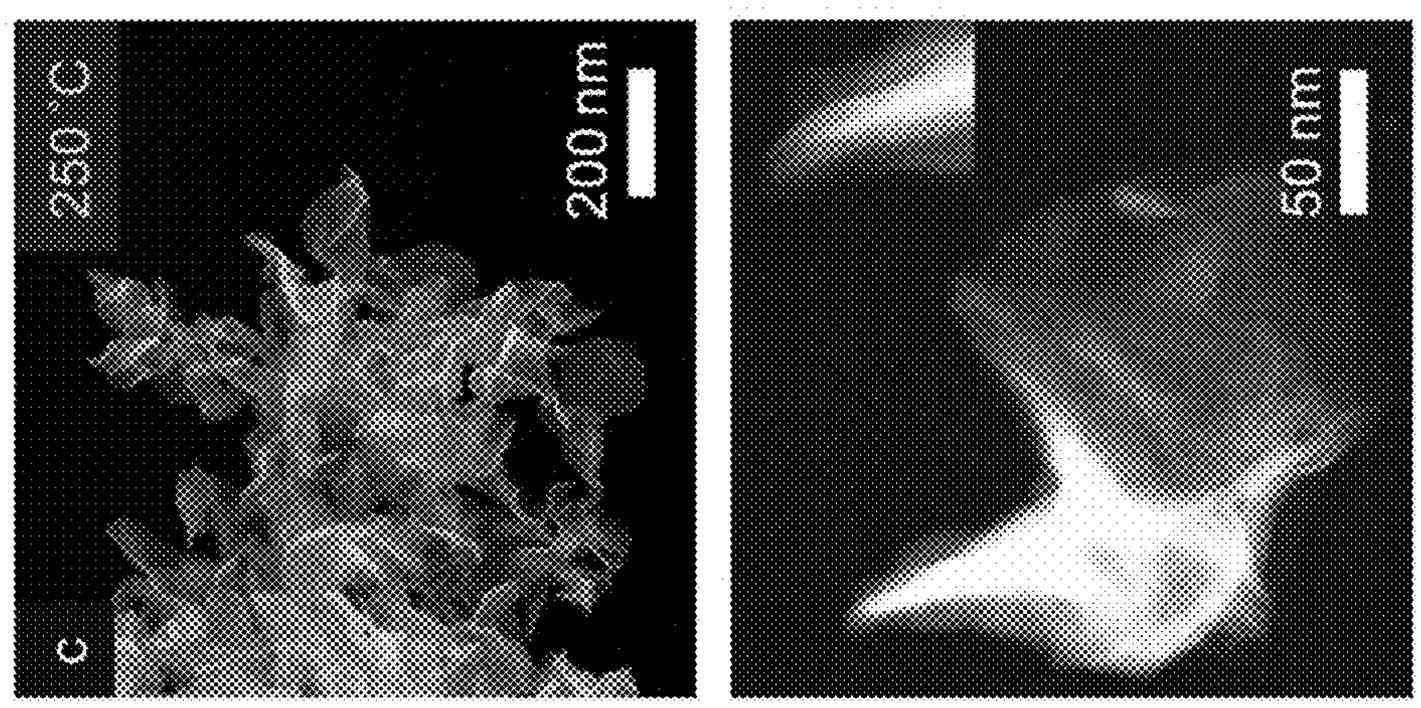

FIG. 5(c)

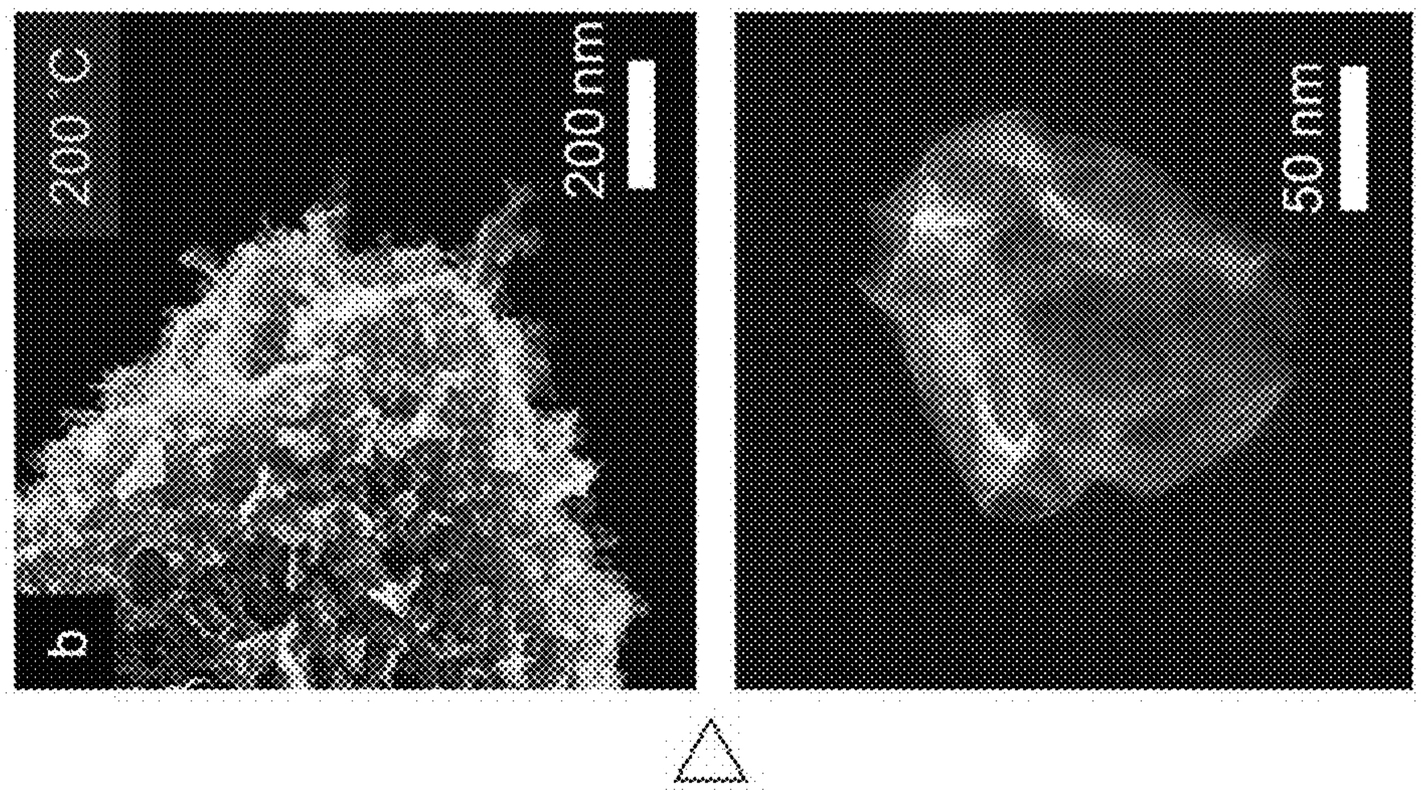

FIG. 5(b)

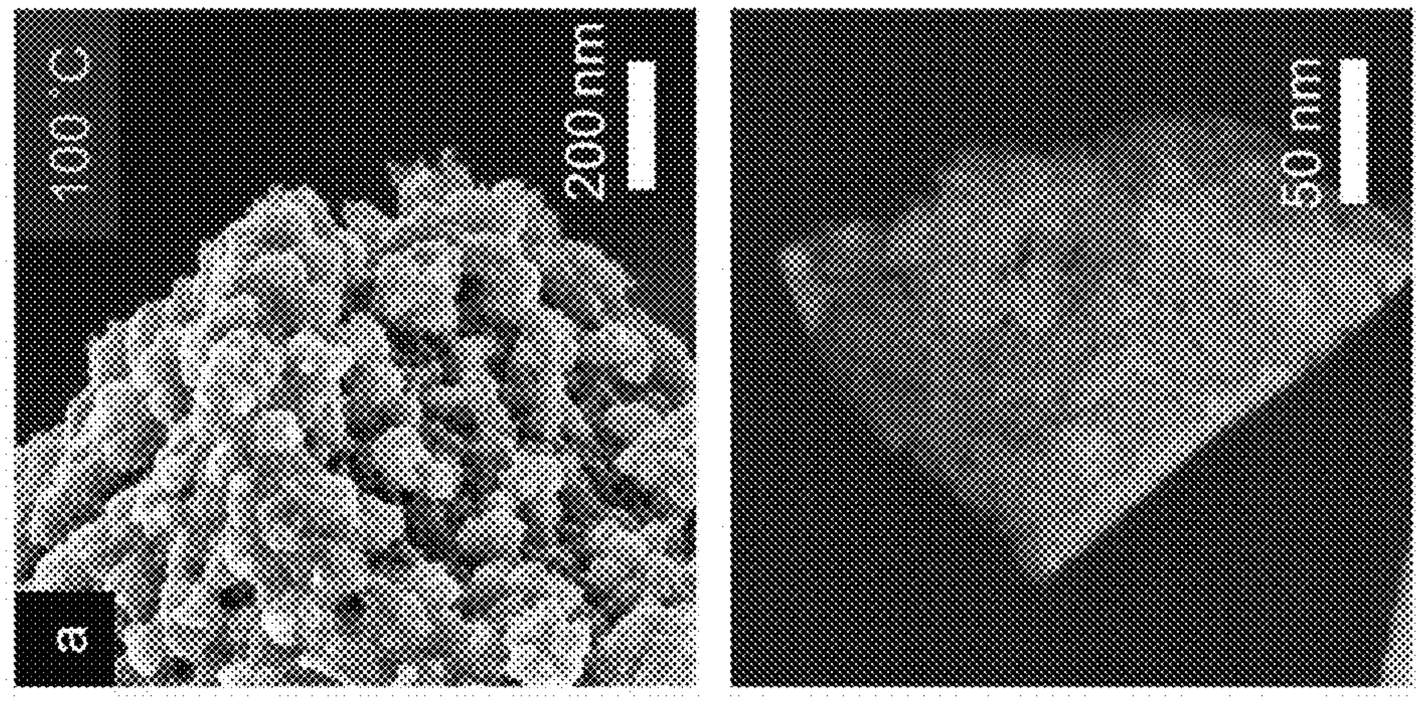

FIG. 5(a)

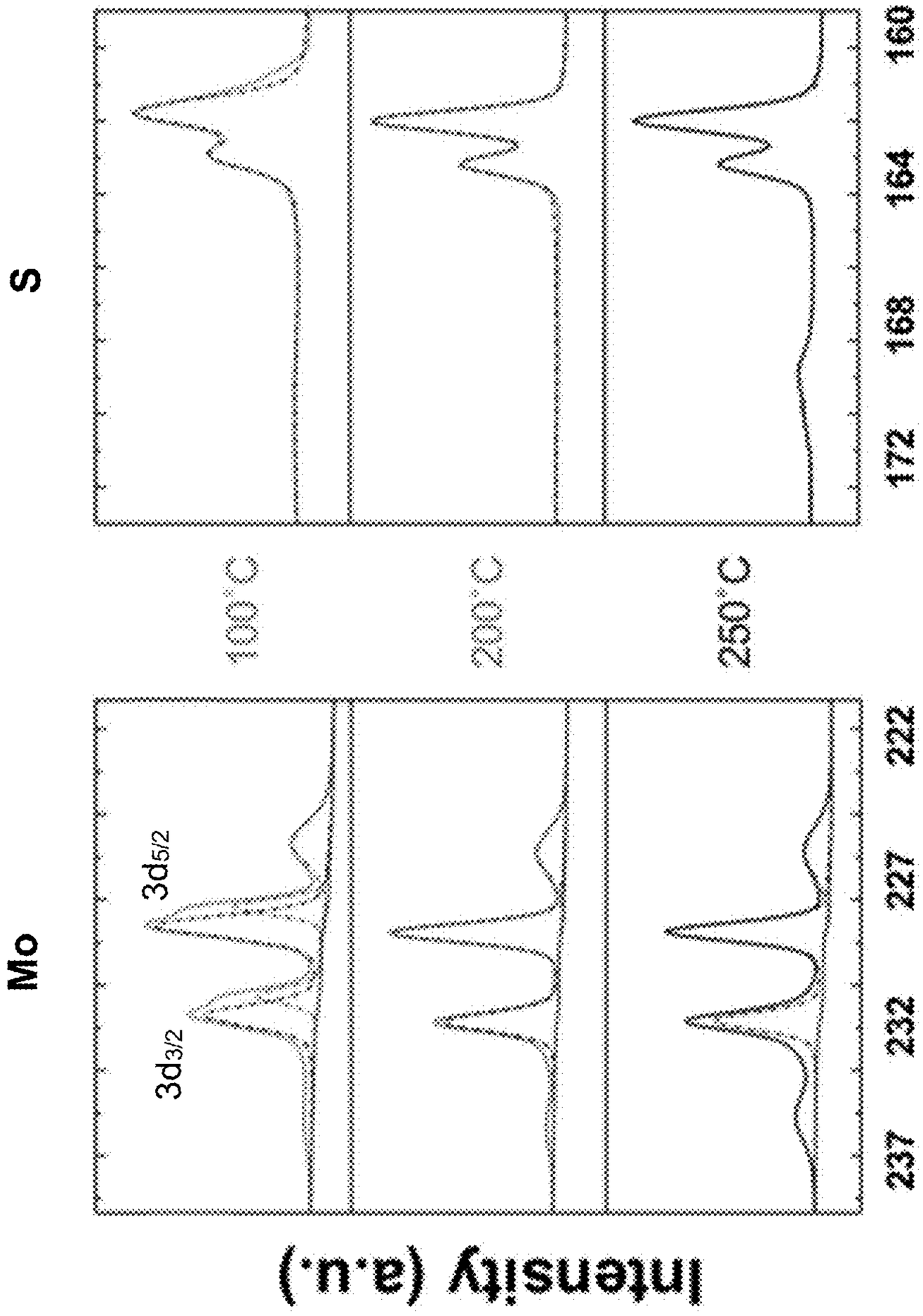
Mo
S
100°C
200°C
250°C
3d5/2
3d3/2
232
227
222
172
168
164
160
237
Binding energy (eV)
Intensity (a.u.)

FIG. 6

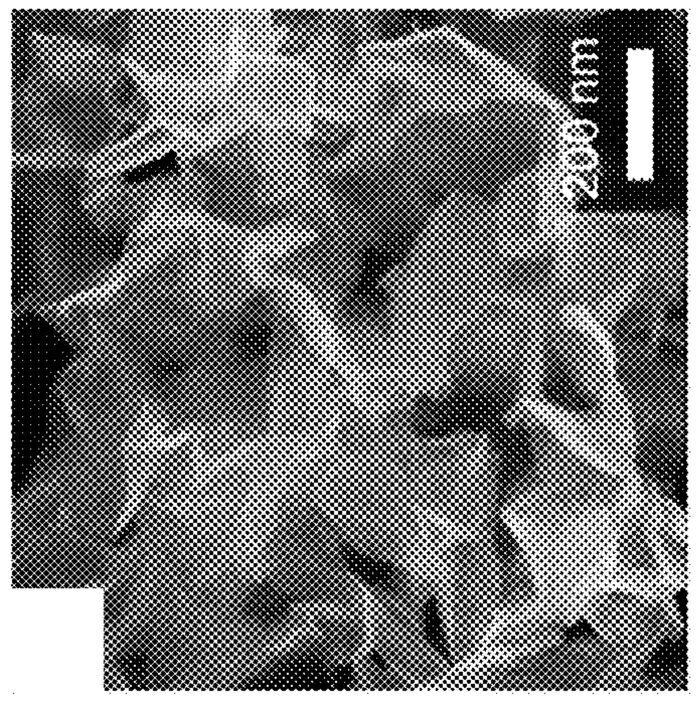

FIG. 7(c)

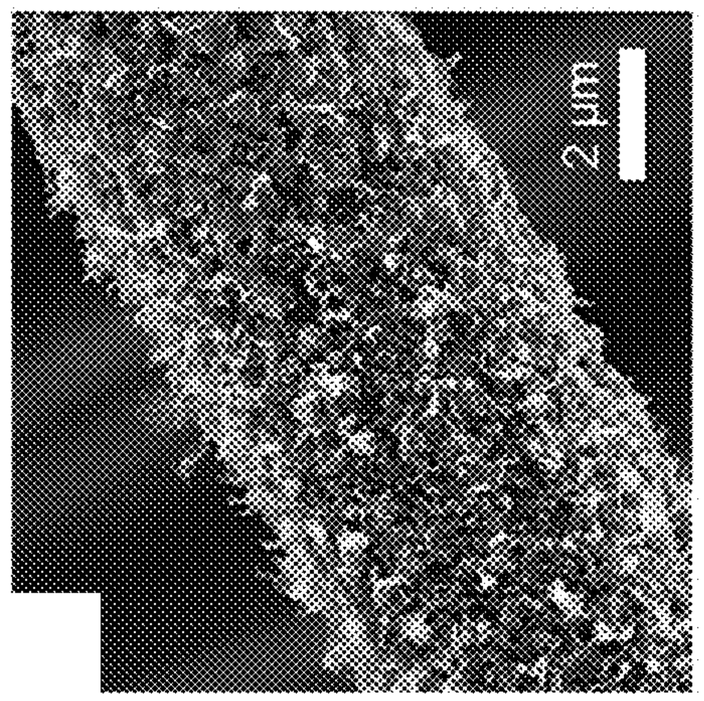

FIG. 7(b)

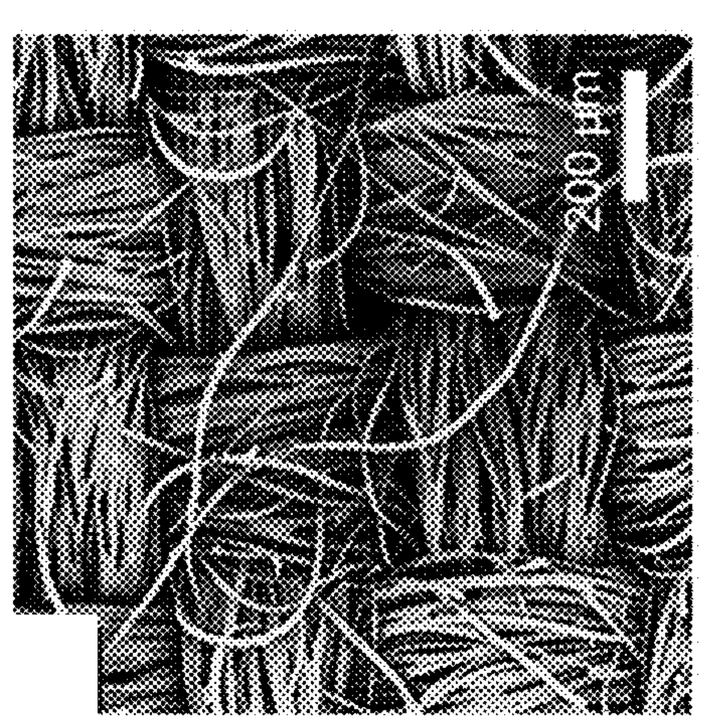

FIG. 7(a)

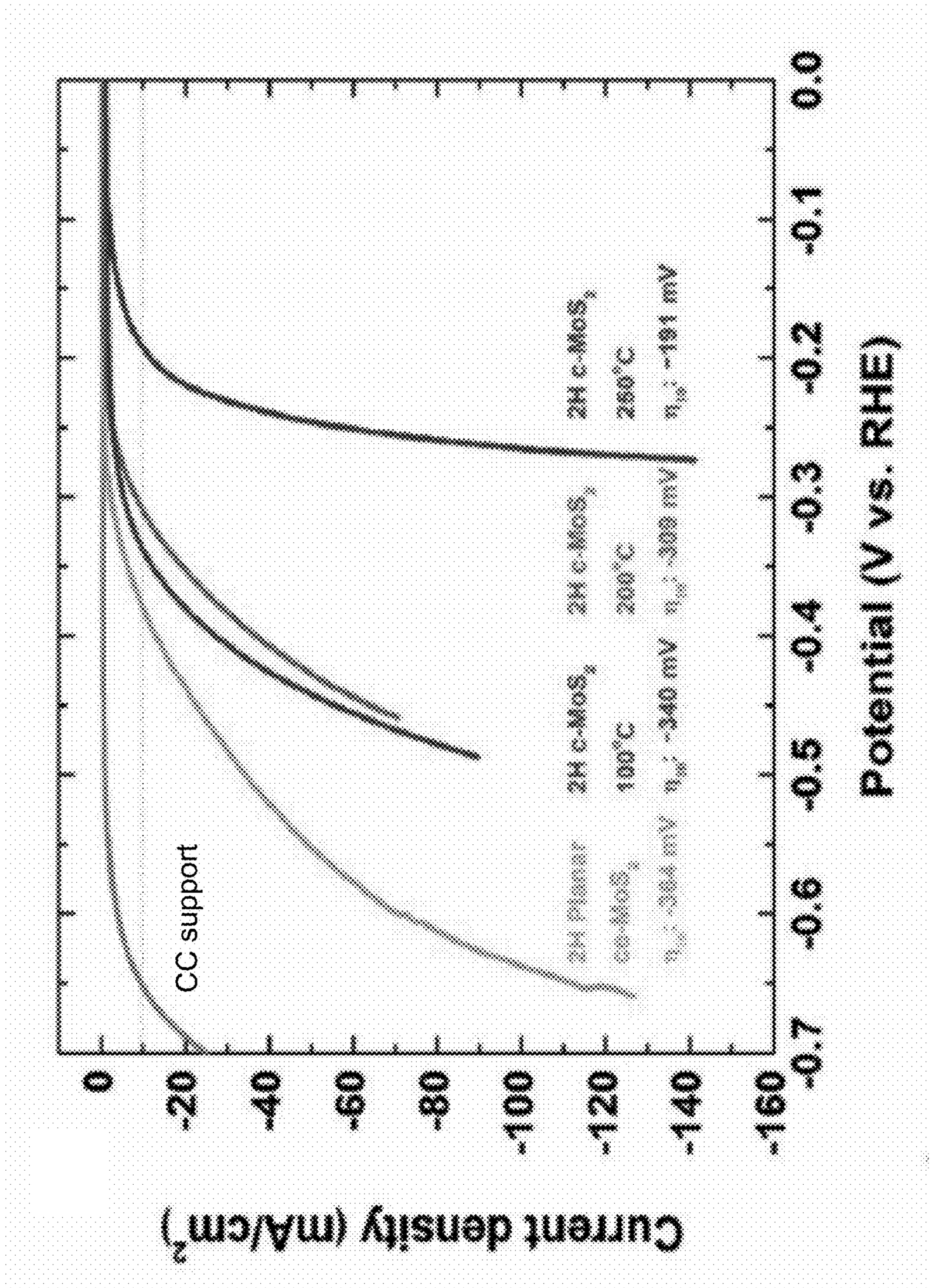
0.0
-0.1
-0.2
-0.3
-0.4
-0.5
-0.6
-0.7
Potential (V vs. RHE)
0
20
40
60
80
100
120
140
160
Current density (mA/cm²)
CC support
2H c-MoS2
2H c-MoS2
2H c-MoS2
2H c-MoS2

FIG. 8

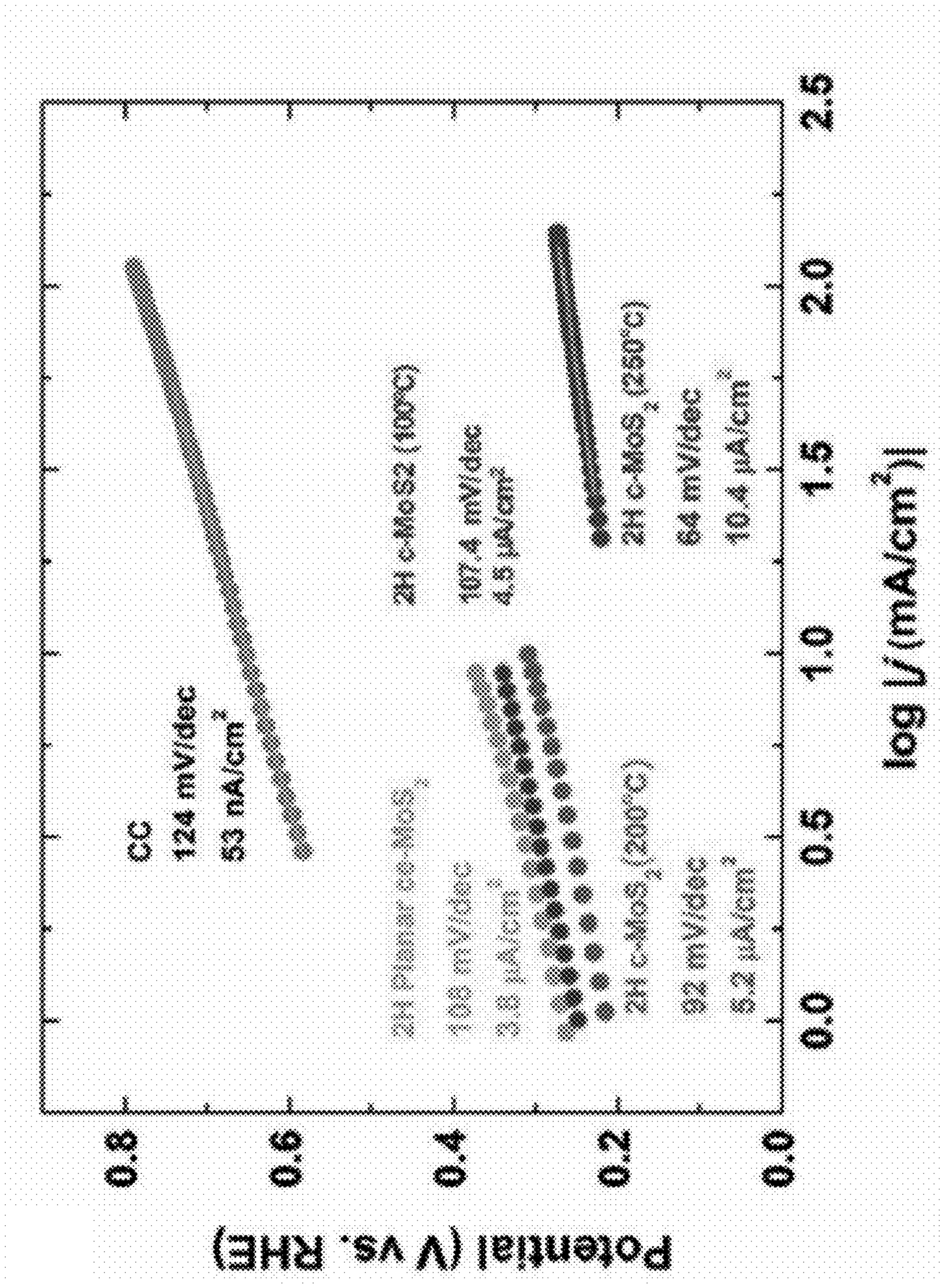
CC
124 mV/dec
53 nA/cm2
2H c-MoS2 (100°C)
107.4 mV/dec
4.5 μA/cm2
2H c-MoS2 (250°C)
64 mV/dec
10.4 μA/cm2
2H c-MoS2 (200°C)
82 mV/dec
6.2 μA/cm2
0.0
0.5
1.0
1.5
2.0
log |j/(mA/cm2)|
Potential (V vs. RHE)

FIG. 9

CRUMPLED TRANSITION METAL DICHALCOGENIDE SHEETS

CROSS-REFERENCE TO RELATED APPLICATION

[0001] This application claims the benefit of U.S. Provisional Application No. 62/526,828, filed Jun. 29, 2017, which is incorporated herein by reference.

STATEMENT OF GOVERNMENT INTEREST

[0002] This invention was made with Government support under Contract No. DE-NA0003525 awarded by the United States Department of Energy/National Nuclear Security Administration. The Government has certain rights in the invention.

FIELD OF THE INVENTION

[0003] The present invention relates to transition metal dichalcogenides and, in particular, to crumpled transition metal dichalcogenide sheets, such as crumpled molybdenum disulfide (MoS_2), that can have catalytic and other applications.

BACKGROUND OF THE INVENTION

[0004] The urgent need to transition the global energy infrastructure away from fossil fuels and toward carbon-neutral sources has propelled a resurgence of research in renewable hydrogen generation. Within this context, there is great interest in the development of hydrogen evolution reaction (HER) electrocatalysts that concurrently possess high total electrode activity (e.g., overpotentials, Tafel slope, and exchange current density) at a low catalyst loading, and tailored intrinsic activity (e.g., turnover frequency (TOF) per active site). See J. D. Benck et al., *ACS Catal.* 4, 3957 (2014). To have widespread impact, such catalytic materials must also be electrochemically stable, thermally robust, and synthetically scalable without the need for specialized processing equipment. While Pt nanoparticles represent the current benchmark for HER electrocatalysis, the elemental scarcity, high cost, and poor stability against nanoparticle coarsening and agglomeration impose practical limitations and motivate the need for a next generation of alternative HER catalysts.

[0005] Molybdenum disulfide (MoS_2), a van der Waals solid composed of adhered-2D monolayers, has emerged as a promising alternative to Pt due to its elemental abundance, high catalytic activity, and electrochemical stability. See J. D. Benck et al., *ACS Catal.* 4, 3957 (2014); J. Greeley et al., *Nat. Mater.* 5, 909 (2006); B. Hinnemann et al., *J. Am. Chem. Soc.* 127, 5308 (2005); and Q. Ding et al., *Chem.* 1, 699 (2016). Despite the various merits of MoS_2, its functional performance remains inferior to that of Pt due to comparatively small active site concentrations as well as its relatively low electrical conductivity. At the root of functional limitations is the inability of MoS_2, in its natural 2H semiconducting phase, to catalyze HER on its inert basal plane, where the Gibbs free energy for hydrogen adsorption (ΔG_H) is exceedingly large. See J. D. Benck et al., *ACS Catal.* 4, 3957 (2014); T. F. Jaramillo et al., *Science* 317, 100 (2017); and J. Kibsgaard et al., *Nat. Mater.* 11, 963 (2012). In contrast, MoS_2 edges possess a favorable ΔG_H, as well as metallic 1D conductivity due to the presence of electronic states in close proximity to the Fermi level. Because of the highly catalytic nature of MoS_2 edges, synthetic approaches that prioritize MoS_2 edges sites over the inert basal plane sites have attracted broad interest. See Q. Ding et al., *Chem.* 1, 699 (2016); T. F. Jaramillo et al., *Science* 317, 100 (2017); J. Kibsgaard et al., *Nat. Mater.* 11, 963 (2012); M.-R. Gao et al., *Nat. Commun.* 6, 7493 (2015); Z. Lu et al., *Adv. Mater.* 26, 2683 (2014); and J. Ekspong et al., *Adv. Funct. Mater.* 26, 6766 (2016). Notable innovations in this area include nanostructured MoS_2 particles, vertically aligned flakes, and wires in conjunction with the engineering of defects, interfacing to conductive scaffolds, and mimicry of the edge structures. See Y. Li et al., *J. Am. Chem. Soc.* 133, 7296 (2011); D. Kong et al., *Nano Lett.* 13, 1341 (2013); Z. Chen et al., *Nano Lett.* 11, 4168 (2011); J. Xie et al., *Adv. Mater.* 25, 5807 (2013); M. A. Lukowski et al., *J. Am. Chem. Soc.* 135, 10274 (2013); G. Ye et al., *Nano Lett.* 16, 1097 (2016); A. J. Smith et al., *Adv. Energy Mater.* 4, 1400398 (2014); Y. H. Chang et al., *Adv. Mater.* 25, 756 (2013); and H. I. Karunadasa et al., *Science* 335, 698 (2012). Yet, despite these innovations, the fundamental inactivity of the MoS_2 basal plane remains a basic material constraint. To enhance catalytic activity, basal plane activation via lithiation and ultrasonication has been used to induce phase transformation into the conductive 1T' MoS_2 polymorph (sometimes termed "metallic," "chemically exfoliated" MoS_2, or ce-MoS_2), which is catalytically active on the basal plane. See M. A. Py and R. R. Haering, Can. *J. Phys.* 61, 76 (1983); S. S. Chou et al., *Nat. Commun.* 6, 8311 (2015); and D. Voiry et al., *Nat. Mater.* 12, 850 (2013). The phase engineering strategy provides a new pathway to drastically enhance the overall HER metrics of 1T' MoS_2 that has been recently extended to WS_2 and $MoSe_2$. See M. a Lukowski et al., *Energy Environ. Sci.* 7, 2608 (2014); and Y. Yin et al., *Adv. Mater.* 29, 1700311 (2017). However, this strategy comes at the cost of reduced robustness, since the 1T' phase is metastable and temperature sensitive. See M. Chhowalla et al., *Nat. Chem.* 5, 263 (2013).

[0006] Beyond phase transformation, basal plane activation via strain engineering has been explored. This approach takes advantage of the shift of the d-band electronic structure with strain, which facilitates a semiconducting-to-metallic phase transformation. See L. Hromadova et al., *Phys. Rev. B: Condens. Matter Mater. Phys.* 87, 1 (2013). However, retention of the metallic phase requires continual application of pressure (≈35 GPa), which is impractical for technological use. See Y.-C. Lin et al., *Nat. Nanotechnol.* 9, 391 (2014); A. P. Nayak et al., *Nat. Commun.* 5, 1 (2014); and Z. H. Chi et al., *Phys. Rev. Lett.* 113, 1 (2014). A hybrid approach using strain on plasma-treated MoS_2 has also been reported, with localized substrate strain plus S vacancies from the plasma treatment shifting its ΔG_H towards thermal neutral (≈0 eV), thus activating the basal plane and enabling HER. See H. Li et al., *Nat. Mater.* 15, 48 (2016); H. Li et al., *Nat. Commun.* 6, 7381 (2015); C. C. Cheng et al., *Nano Energy* 30, 846 (2016); and G. Li et al., *J. Am. Chem. Soc.* 138, 16632 (2016). However, as strain here is derived from lithographically defined substrate topography, it is potentially too costly for production. See H. Li et al., *Nat. Commun.* 6, 7381 (2015). Furthermore, because the product is inherently planar, it has limited prospects for integration in multilayer systems, which is a practical need for many applications and constrains device architectures. Most recently, the basal plane of MoS_2 has also been "activated" by improving substrate/electron transport to defects within

MoS_2 sheets. See D. Voiry et al., *Nat. Mater.* 15, 1003 (2016). However, this method similarly requires lithography and patterning, rendering scalability a challenge. It should also be noted that the 1T', the strained S-vacancy, and the electronic coupling approaches to basal plane activation are all limited to extremely thin specimens to 2 layers), thus limiting the number of active sites and making scalable integration difficult.

SUMMARY OF THE INVENTION

[0007] The present invention is directed to a method of crumpling transition metal dichalcogenide sheets, comprising forming an electrostatically charged liquid droplet comprising a plurality of planar sheets of a transition metal dichalcogenide; applying a sufficient electric field to the droplet to cause the droplet to rupture into a plurality of fission droplets by an electrohydrodynamic process, wherein each fission droplet comprises at least one planar sheet of the transition metal dichalcogenide; and evaporating the remaining liquid from the plurality of fission droplets, thereby inducing spontaneous self-crumpling of the at least one planar sheet of the transition metal dichalcogenide in each of the fission droplets.

[0008] The invention provides a facile and high throughput method for obtaining electrochemically stable, thermally robust, and highly efficient HER catalysts via electrohydrodynamic (EHD) induced dimensional transition of 2D planar ce-MoS_2 sheets into 3D structurally deformed MoS_2 nanostructures, namely crumpled MoS_2 (c-MoS_2). The material, obtained from EHD-assisted crumpling, electrostatically isolates and then transforms individual ce-MoS_2 sheets into 3D crumpled architectures, provides highly accessible and electrochemically active surface-area (310.8+/−0.5 m^2 g^{-1} and catalytic site density of 5.86×10^{17} sites cm^{-2}) that allows infiltration of electrolytes to the fully exposed active sites on the activated basal plane and edges while allowing efficient charge transfer between electrolyte, activated basal plane and edges, as confirmed by a substantially reduced charge-transfer resistance (R_{ct}). Meanwhile, the hierarchically strained conformational features, including facets, folds, ridges, vertices, and wrinkles, can substantially reduce the series resistance (R_s), closely resembling the orbital effect induced by regions of atomically localized curvature in nanocarbon allotropes and textured MoS_2. See S. Luo et al., *Nanotechnology* 26, 105705 (2015); and D. Srivastava et al., *J. Phys. Chem. B* 103, 4330 (1999). In addition, the synergistic combination of high strain load emanating from structurally deformed morphology and spatially distributed S vacancies intrinsic to the chemical exfoliation process collectively tailors the 2H basal plane with a catalytically and thermodynamically favorable environment, as confirmed by the improved TOF of 0.130 H_2 molecules per second. See D. Srivastava et al., *J. Phys. Chem. B* 103, 4330 (1999). The net result is much enhanced HER activity with a Tafel slope of 64 mV per dec, exchange current density of 10.4 μA cm^{-2}, high cathodic current density (>100 mA cm^{-2} at less than −300 mV), and an overpotential (η_{10}) of −191 mV to achieve a current density of −10 mA cm^{-2} at an exceedingly low aerial mass loading of only 13 μg cm^{-2}. The significantly enhanced intrinsic and total electrode HER characteristics compare favorably with state-of-art MoS_2 catalysts while using a fully scalable and easy to integrate material process. See J. Kibsgaard et al., *Nat. Mater.* 11, 963 (2012); M.-R. Gao et al., *Nat. Commun.* 6, 7493 (2015); Y. Li et al., *J. Am. Chem. Soc.* 133, 7296 (2011); D. Kong et al., *Nano Lett.* 13, 1341 (2013); M. A. Lukowski et al., *J. Am. Chem. Soc.* 135, 10274 (2013); G. Ye et al., *Nano Lett.* 16, 1097 (2016); H. Li et al., *Nat. Mater.* 15, 48 (2016); and D. Voiry et al., *Nano Lett.* 13, 6222 (2013). More importantly, the structurally deformed MoS_2, with in situ strain fields propagating on the thermodynamically favored 2H phase, demonstrates consistent HER characteristics under continuous operations of 5000 cycles or annealing at high temperatures (up to 300° C.), enabling effective integration into fuel cell and other applications.

BRIEF DESCRIPTION OF THE DRAWINGS

[0009] The detailed description will refer to the following drawings, wherein like elements are referred to by like numbers.

[0010] FIG. **1**(*a*) is a schematic illustration the chemical exfoliation of bulk MoS_2 powder. FIG. **1**(*b*) is a transmission electron microscope (TEM) image of the exfoliated MoS_2, showing internal edges which increase overall edge density. FIG. **1**(*c*) is a high-angle annular dark-field scanning transmission microscope (HAADF-STEM) image, showing spatially distributed atomistic point defects, including single and double sulfur vacancies (V_{S1}, V_{S2}), Mo anti-site substitutions (Mo_{S2}) and S anti-site substitutions ($S2_{Mo}$).

[0011] FIG. **2** is a schematic illustration of EHD-assisted crumpling of exfoliated MoS_2, showing that chemical exfoliation also facilitates stable colloidal dispersions of ce-MoS_2 within the EHD-generated droplets that can be viewed as charged, noncolloidal reactors. Under a high electric field, the reactant, 2D ce-MoS_2, within these nanoreactors undergoes stages of (i) electrostatically induced separation, (ii) fission, and (iii) capillarity-induced self-crumpling into 3D c-MoS_2.

[0012] FIG. **3**(*a*) is a transmission electron microscope (TEM) image of the 3D c-MoS_2. FIG. **3**(*b*) is a high-resolution transmission electron microscope (HRTEM) image showing extremely thin layers because of electrostatic forces and fission. FIG. **3**(*c*) is an HRTEM image showing sharp vertices and facets with radii of curvatures at nanoscale. FIG. **3**(*d*) is an HRTEM image showing propagating ridges.

[0013] FIG. **4** is a graph of Raman spectra showing a progressive red shift of the E^1_{2g} with increased deposition temperature, indicating a progressively strained morphology.

[0014] FIG. **5**(*a*) shows SEM and HRTEM images of MoS_2 deposited at 100° C., revealing rugged island like morphology and relatively flat, featureless basal plane with slightly corrugated folds around the edges when isolated. FIG. **5**(*b*) shows SEM and HRTEM images of EHD deposition at 200° C. coincides with emergence of wrinkled sheets. FIG. **5**(*c*) shows SEM and HRTEM images of MoS_2 deposited at 250° C., showing fully realized individual crumples with porous structures, and highly rippled edges were observed.

[0015] FIG. **6** is an XPS spectra of the Mo 3d (left) and S 2p (right) peaks showing mixed 1T' and 2H XPs signatures in samples deposited at 100° C. and pure 2H phase at 200° C. and 250° C.

[0016] FIGS. **7**(*a*) and **7**(*b*) are SEM images showing the uniform and full coverage of c-MoS_2 supported on CC using EHD deposition at different scales. FIG. **7**(*c*) is an HRSEM

image providing a close-up view of densely packed crumpled MoS_2 assemblies with porous morphology and highly curved edges.

[0017] FIG. **8** is a graph of linear sweep voltammogram (LSV) curves for the carbon cloth (CC) scaffolds, a planar 2H MoS_2 sheet, crumpled MoS_2 deposited at 200° C., and crumpled MoS_2 prepared at 250° C. Overpotentials required to reach current densities of −10 mA/cm^2 are labeled.

[0018] FIG. **9** is a graph of Tafel plots corresponding to the LSV curves. The plots are labeled with Tafel slopes and exchange current densities, showing much improved total electrode HER characteristics at an exceedingly low mass loading of crumpled MoS_2.

DETAILED DESCRIPTION OF THE INVENTION

[0019] FIG. **1**(*a*) is a schematic illustration of the synthesis of single layer ce-MoS_2 by a modified Li-intercalation followed by ultrasonic exfoliation. See M. B. Dines, *Mater. Res. Bull.* 10, 287 (1975); and G. Eda et al., *ACS Nano* 6, 7311 (2012). In the example described below, a prolonged reaction time of 96 h resulted in the conversion of 64% of trigonal prismatic coordination (2H phase) into octahedral coordination (1T' phase). High resolution transmission electron microscopy (HRTEM) revealed that the basal plane of the resultant ce-MoS_2 can be readily addressed with significant tears in the 10-nm scale that affords edge-like structures, as shown in FIG. **1**(*b*). Additionally, as shown in FIG. **1**(*c*), high-angle annular dark field (HAADF) and aberration-corrected scanning transmission electron microscopy (STEM) images reveal atomically resolved point defects including S vacancies (V_S), Mo anti-site substitution (Mo_s), and Mo vacancies (V_{Mo}), mono in tandem with bi-sulfur vacancies (V_{S1}, V_{S2}) and antisite substitutions within MoS_2. See J. Xie et al., *Adv. Mater.* 25, 5807 (2013). Detailed analysis of the MoS_2 basal plane with lateral dimensions of 6.75 nm×6.75 nm (estimated from the lattice distance of 3.16 Å) revealed that the large majority of the defects consist of V_S with a total number about 79 (out of 440 Mo atoms, ≈9% S-vacancies). Theoretical calculations indicate that S vacancies as low as ≈3% lowers ΔG_H from more than 2 eV down to nearly 0.2 eV. See H. Li et al., *Nat. Mater.* 15, 48 (2016). The average S-vacancy percentage over 8 such areas was calculated to be 9.3+/−1.7%, thus creating a catalytically active basal plane. Although continuous modulation of ΔG_H toward thermal neutral can be made possible by mounting up the number of S-vacancies, the overall structural integrity of ce-MoS_2 sheets is at the mercy of fragmentation.

[0020] To further modulate the ΔG_H of ce-MoS_2 sheets while preserving the structural integrity, an EHD process was adapted, which is typically employed for generating ultrafine droplets in high throughput thin film production. See H. Ishihara et al., *Sci. Rep.* 6, 38701 (2016); H. Ishihara et al., *Adv. Mater. Interfaces* 3, 1 (2016); and H. Ishihara et al., *J. Mater. Chem. A* 4, 6989 (2016). As shown in FIG. **2**, under a high electric field, the liquid medium deforms and then disintegrates into self-dispersing, charged droplets, providing electrostatically stabilized colloidal systems that inhibit ce-MoS_2 sheets from restacking. The EHD deposition is characterized by a droplet fission process, in which surface charge density drastically increases during solvent-evaporation-induced volumetric shrinkage, ultimately reaching the Rayleigh limit. At this point, electrostatically charged droplets rupture into smaller ones with a diameter distribution in the sub-micrometer range. Thus, each fine droplet contains single- to few-layered ce-MoS_2 sheets before proceeding to a final stage of self-crumpling. In addition to being a dispersing medium, these individualized, charged colloidal droplets can be considered soft templates that impose capillarity-induced geometric constraints to induce the crumpling of ce-MoS_2 sheets upon evaporation. Therefore, ce-MoS_2 within these charged droplets will first separate into approximately individual sheets before being compressed into crumpled nanostructures.

[0021] The method of EHD-assisted crumpling can generally be applied to the crumpling of any transition metal dichalcogenide sheet. Transition metal dichalcogenide sheets are atomically thin semiconductors of the type MX_2, where M is a transition metal atom (e.g., Mo, W) and X is a chalcogenide atom (e.g., S, Se, Te). The sheets comprise a layer of M atoms sandwiched between two layers of X atoms, typically in a hexagonal structure. Bulk crystals of transition metal dichalcogenides comprise monolayer sheets that are bound to each other via weak Van-der-Waals attraction. Therefore, MX_2 monolayers can be obtained by exfoliation of the bulk crystal, either by mechanical abrasion or by liquid-phase exfoliation. Alternatively, monolayer MX_2 can be grown by chemical vapor deposition or molecular beam epitaxy. These MX_2 sheets can be crumpled following the same EHD process described above.

EXAMPLE

Lithium Intercalation and Exfoliation and MoS_2 Crumpling by EHD

[0022] As an example of the invention, Li-intercalation was accomplished by immersing 2 g of MoS_2 powder in 15 mL of 0.8 m n-butyl lithium in hexane. The mixture was stirred vigorously in an Ar-filled glovebox for 96 h. Next, the intercalated compound was transferred to DI-H_2O and sonicated to yield exfoliated monolayers. Upon contact with the DI-H_2O, copious gas evolved at the interlayer interfaces, thus yielding high concentrations of monolayers and forming a black, opaque solution. After ultrasonication, the compound was washed over Whatman filter paper with 500 mL of hexane. 200 mL of DI-H_2O was then added to the mixture. With the filter paper removed, the mixture was then sonicated for 90 min. The resulting solution was then aliquoted into 45 mL centrifuge tubes with solution depths of 2-3 cm and centrifuged at 5200 rcf for 12 h, decanted, and then resuspended in 100 mL of DI-H_2O. After resuspension, the centrifugation procedure was repeated twice, followed by resuspension in 50 mL and, later, 25 mL of water. The resulting ce-MoS_2 was further diluted to 250 μg mL^{-1} in a mixture of DI water and isopropyl alcohol (DI-H_2O: IPA=7:3, v/v) for subsequent EHD crumpling.

[0023] To prepare c-MoS_2 with the highest strain (≈3.7%), a hot plate was pre-annealed at 250° C. for 60 min prior to deposition. Next, aqueous solutions of ce-MoS_2 (250 μg mL^{-1}) were fed to a spinneret (gauge 18 TW needle) by a programmable syringe pump. An external electric field of 1.25 kV cm^{-1} was generated with a high-power supply. Computerized multi-pass deposition onto pre-cleaned carbon cloth (CC) HER electrodes was achieved through the integration of an x-y translational stage at a linear stage speed of 2.5 mm s^{-1}. The flow rate and surface temperature were carefully maintained at 25 μL min^{-1} and 250° C., respectively, to achieve the high yield of c-MoS_2. The

amount of deposited c-MoS_2 catalyst was ≈13 μg cm^{-2}. Deposition yield was found to linearly scale with the concentration of ce-MoS_2 dispersions, flow rate, and duration of EHD process.

[0024] Scanning electron microscopy (SEM) and atomic force microscopy (AFM) images revealed largely separated and spatially distributed ce-MoS_2 sheets with average thickness in the range of nm when the threshold electric field reached 1.25 kV cm^{-1} for the inception of the fission process. This result confirms that electrostatic stabilization prevents unwanted aggregation. Furthermore, ce-MoS_2 was found to spontaneously crumple into 3D porous, structurally deformed nanostructures with many wrinkles, ridges, and corrugated edges upon reaching both the threshold electric field of 1.25 kV cm^{-1} and a deposition temperature of 250° C., as suggested in the TEM image shown in FIG. **3**(*a*). HAADF and STEM images collectively showed that the resulting c-MoS_2 deposited at 250° C. comprises a predominant 2H phase because the deposition temperature exceeded the temperature for transformation of the metastable 1T' phase to the 2H phase. See G. Eda et al., *ACS Nano* 6, 7311 (2012); and S. S. Chou et al., *J. Am. Chem. Soc.* 137, 1742 (2015). The impact of the EHD-assisted crumpling process on the structure of c-MoS_2 at the nanoscale was further probed using HRTEM. The HRTEM image in FIG. **3**(*b*) pinpoints areas near edges. FIGS. **3**(*c*) and **3**(*d*) show areas on the basal plane. The edges of c-MoS_2 consist of only few layers, as determined by the clear steps in the relatively flat region, whereas propagating ridges along with sharp vertices, and facets can also be clearly identified, thus creating localized conformational strain with radii of curvature of nanometer scale.

[0025] Raman spectroscopy substantiates the c-MoS_2 structures by tracing the evolution of two distinct peaks at 385 and 407 cm^{-1}, assigned to the E^1_{2g} and A^1_g phonon modes of the 2H planar ce-MoS_2, respectively, as a function of processing temperatures, shown in FIG. **4**. See S. S. Chou et al., *J. Am. Chem. Soc.* 137, 1742 (2015). At higher deposition temperatures, a much more pronounced out-of-plane Mo—S A^1_g phonon was observed, along with a significant red shift of the in-plane Mo—S E^1_{2g} phonon mode. In the former, the enhancement of the A^1_g mode is characteristic of exposed edges that preferentially align with the polarization of the exciting laser. See D. Kong et al., *Nano Lett.* 13, 1341 (2013). Additionally, the relatively small E^1_{2g} to A^1_g ratio (≈0.5) is an indication of both small domain size and textured morphology. This is not surprising since the crumpling process concurrently induces volumetric shrinkage of ce-MoS_2 and surface texturing of the resultant film. The E^1_{2g} phonon mode, however, did not shift toward a lower wavenumber relative to the planar 2H ce-MoS_2 even though the overall morphology appears to be heavily wrinkled at a deposition temperature of 100° C. Instead, a pronounced red shift of the E^1_{2g} mode toward lower wavenumbers only took place in the specimens synthesized at temperatures higher than 200° C. The shift of the E^1_{2g} phonon mode provides an index for quantifying surface strain load and has been shown to shift by ≈1.7 cm^{-1} per % strain on the MoS_2. See A. Castellanos-Gomez et al., *Nano Lett.* 13, 5361 (2013). Here, c-MoS_2 synthesized at 100° C. did not yield a significant E^1_{2g} shift, and thus strain, whereas the E^1_{2g} peak of c-MoS_2 synthesized at 200° C. was red shifted by 2 cm^{-1} (≈1.2% of strain). The E^1_{2g} phonon mode further redshifted for c-MoS_2 formed at 250° C., generating an average strain load of ≈3.7%. For reference, this strain is comparable to that reported by Zheng and co-workers for modulating S-deficient MoS_2 basal planes. See H. Li et al., *Nat. Mater.* 15, 48 (2016).

[0026] To better correlate morphology with the observed strain induced E^1_{2g} shift, the morphological evolution of c-MoS_2 deposited on carbon cloth (CC) was analyzed as a function of deposition temperature. As described above, ce-MoS_2 sheet precursors aggregated into discrete, rugged islands at the low deposition temperature of 100° C. Nevertheless, TEM image reveals that individual ce-MoS_2 sheets display a relatively flat and featureless morphology with slightly corrugated folds around the edges, as shown in FIG. **5**(*a*). Comparatively, aggregated clumps begin to disintegrate into largely buckled structures with the emergence of thin, vertically protruding walls, meandering ridges, curled edges, and folds when processed at 200° C., as shown in FIG. **5**(*b*), matching the onset of the red shift in the E^1_{2g} phonon mode and the corresponding moderate strain load. At 250° C., almost all the ce-MoS_2 sheets were transformed and compressed into 3D structurally deformed nanostructures with petal-like, curved morphology, as shown in FIG. **5**(*c*), and thus the high magnitude of strain, an important feature necessary for further modulating the ΔG_H. See J. D. Benck et al., *ACS Catal.* 4, 3957 (2014); and H. Li et al., *Nat. Mater.* 15, 48 (2016). In particular, the hierarchically crumpled MoS_2 at 250° C. reveals a highly strained c-MoS_2 that comprises corrugated edges and extremely thin layers, narrow folds converged to form propagating ridges, and sharp vertices and facets with radii of curvatures at nanoscale. Rich and spatially distributed defects are throughout.

[0027] In parallel, the chemical states of Mo and S were investigated by X-ray photoelectron spectroscopy (XPS) on c-MoS_2 synthesized at different temperatures, as shown in FIG. **6**. Deconvolution of the Mo 3d core level region from c-MoS_2 synthesized at 100° C. showed additional peaks at 228.1 eV (Mo $3d_{5/2}$) and 231.3 eV (Mo $3d_{3/2}$), relative to pure 2H MoS_2, which exhibited peaks at 229.1 eV (Mo $3d_{5/2}$) and 232.2 eV (Mo $3d_{3/2}$). The presence of these additional core level photoemission peaks indicates the presence of the 1T' phase and integrated peak area ratios reveal a 2H phase fraction of 76% for c-MoS_2 synthesized at 100° C. See S. S. Chou et al., *J. Am. Chem. Soc.* 137, 1742 (2015); and J. Heising and M. G. Kanatzidis, *J. Am. Chem. Soc.* 121, 11720 (1999). Images obtained through HRTEM, along with false-colored HAADF, confirm the coexistence of both phases at a deposition temperature lower than that of phase transformation (100° C.), which is consistent with the spectroscopic interpretation. In contrast, a phase transition to pure 2H material was observed when c-MoS_2 was processed at 200° C. The predominant 2H to 1T' ratio remained constant at 250° C., demonstrating stable 2H crumpling. As shown in the right-hand panels in FIG. **6**, complementary analysis of S 2p core-level spectra corroborate these results.

[0028] These c-MoS_2 films maintained mesoporosity, as indicated by Brunauer-Emmett-Teller (BET) isotherms (surface area of 310.8+/−0.5 m^2 g^{-1}). This is notable because the combination of electrostatic stabilization and subsequent fission effectively suppresses the formation of large clumps, enabling 3D integration with HER accessible surfaces and micropores. Moreover, in a similar fashion to a paper ball, the deformed ridges made of several overlapping folds form structural supports that prevent the c-MoS_2 from unfolding

or collapsing when subjected to external stimuli. Indeed, structurally robust c-MoS_2 can sustain common material processing conditions, such as solution processing, high temperature annealing, or the combination of both, and still maintain a porous, nanotextured morphology necessary for preserving efficient transport of H^+ and H_2 to the edge sites and activated basal plane under continuous electrochemical operation or elevated temperate. Together with the strained S vacancies, these structural features, revealed by the Raman, BET, SEM, and TEM characterizations described above, indicate that c-MoS_2 can be used as a catalytically active, electrochemically and thermally stable component for HER.

[0029] The use of an EHD process offers the distinct advantage to directly integrate c-MoS_2 into diverse device architectures, as well as onto a variety of substrates, including thin films of carbon nanotubes (CNTs), silicon, and even nanostructured polystyrene, in both monolithic and a selective fashion. To evaluate the catalytic performance of c-MoS_2 for HER, electrodes were formed by depositing thin films of c-MoS_2 onto CC via EHD deposition, as described above. The substrate had an area of 1 cm^2 and the total aerial mass loading was ≈13 μg cm^{-2}. In FIGS. **7**(*a*)-(*b*), it can be seen that densely packed c-MoS_2 assemblies are uniformly distributed throughout the entire carbon clothes (CC). FIG. **7**(*c*) further suggests that mesoporous c-MoS_2 structures remains intact and retains a high degree of crumpling even upon continuous deposition. In addition, corresponding energy-dispersive X-ray (EDX) mapping of relevant elements (not shown), including Mo and S, closely overlap the contours and areas of c-MoS_2 and underlying CC substrates.

[0030] The HER cathodes made of c-MoS_2 supported on CC were examined using a standard three-electrode electrochemical configuration in 0.5 m H_2SO_4 electrolyte deaerated with Ar. Following deposition and prior to measurement, all samples were annealed at 250° C. for 1 h to ensure complete conversion of remnant 1T' phases to 2H phases. This provides a well-defined system to unambiguously explore the correlation between the impact of 3D nanostructures, strain-induced modulation, and the catalytic activity in phase pure c-MoS_2. To this end, linear sweep voltammograms (LSVs) were measured from thin films of planar 2H ce-MoS_2 standard (S vacancies, strain: 0%, and heavily aggregated morphology), c-MoS_2 synthesized at 100° C. (S vacancies, strain: 0%, and rippled morphology), c-MoS_2 synthesized at 200° C. (S vacancies, strain: 1.2%, and partially crumpled morphology), and c-MoS_2 synthesized at 250° C. (S vacancies, strain: 3.7%, and 3D fully crumpled morphology), along with the bare CC support as a reference, as shown in FIG. **8**. CC electrodes did not show any pronounced cathodic current, and remained inactive during LSV scans. The planar 2H ce-MoS_2 standard electrodes showed very poor HER characteristics even with a high density of S vacancies that have shown to activate the basal plane, delivering an exceedingly high η_{10} of ≈−364 mV. This poor HER performance can be attributed to the lack of electronic coupling between the substrates and active sites in combination with a heavily aggregated morphology that limits the exposure of activated basal plane toward HER. See H. Li et al., *Nat. Mater.* 15, 48 (2016). Meanwhile, increasing the deposition temperature to 100° C. led to the formation of a rippled morphology and η_{10} was reduced to −340 mV. The η_{10} of the c-MoS_2 synthesized at 200° C. was significantly reduced to −309 mV due to the presence of wrinkled morphology and moderate strain load (≈1.2%). Importantly, c-MoS_2 synthesized at 250° C., which was characterized by a combination of high strain load (≈3.7%) and 3D, fully crumpled nanostructures, displayed substantially improved total electrode metrics, including η_{10} of −191 mV, exchange current densities of 10.4 μA cm^{-2}, and high cathodic current densities.

[0031] Further insights into function were obtained by extracting slopes from the Tafel plots shown in FIG. **9**. Tafel slopes were found to decrease with increasing magnitude of crumpling, and were correlated with the strain load. The lowest Tafel slope of 64 mV per dec was obtained for the c-MoS_2 synthesized at 250° C., suggesting a Heyrovsky mechanism at the surface of c-MoS_2 with the hydrogen desorption reaction as the limiting step: $H_{ads}+H_3O^++e^- \rightarrow H_2+H_2O$. See J. D. Benck et al., *ACS Catal.* 4, 3957 (2014); M. A. Lukowski et al., *J. Am. Chem. Soc.* 135, 10274 (2013); B. E. Conway and B. V. Tilak, *Electrochim. Acta* 47, 3571 (2002); and C. Tsai et al., *Surf. Sci.* 640, 133 (2015). Note that total electrode activities are typically commensurate with the catalyst loading, as shown in Table 1. See J. D. Benck et al., *ACS Catal.* 4, 3957 (2014). Thus, from a practical perspective, the ability to deliver compelling total electrode characteristics on a HER electrode with very low loadings of c-MoS_2 catalysts per geometric area (≈13 μg cm^{-2}) may be transformative and economically viable.

[0032] The active site numbers were further estimated using the underpotential deposition (UPD) method. See A. Y. Lu et al., *Small* 12, 5530 (2016); and C. L. Green and A. Kucernak, *J. Phys. Chem.* 2, 11446 (2002). The density of active sites was determined to be approximately 1×10^{14} sites cm^{-2} for planar 2H ce-MoS_2, increased to 5.7×10^{16} sites cm^{-2} for planar 1T' ce-MoS_2 polymorph, and further increased to 5.86×10^{17} sites cm^{-2} for 2H c-MoS_2, thus corroborating that the advent of the hierarchically structured, 3D morphology of c-MoS_2 from the intrinsically planar morphology of ce-MoS_2 and enabling infiltration of electrolyte for exposure to both activated basal plane and edges. See J. Kibsgaard et al., *Nat. Mater.* 11, 963 (2012); D. Kong et al., *Nano Lett.* 13, 1341 (2013); and H. Wang et al., *ACS Nano* 8, 4940 (2014). The effective electrochemically active surface area, deduced from the electric double-layer capacitance (EDLC), increased by 12× when the c-MoS_2 was deposited at 100° C., 24× when the c-MoS_2 was deposited at 200° C., and by 125x when deposited at 250° C. relative to that of planar 2H ce-MoS_2 annealed at 250° C. Meanwhile, electrochemical impedance spectroscopy (EIS) also suggested that the 3D porous morphology facilitates efficient transport across the electrode/electrolyte interfaces as indicated from the substantially reduced R_{ct} (13Ω of 2H c-MoS_2) relative to that of the planar 2H ce-MoS_2 (R_{ct}=275Ω, Table 1). Additionally, the measured R_s was significantly reduced from 38Ω (planar 2H ce-MoS_2) to 1.5Ω (2H c-MoS_2). This is unexpected, since the 2H c-MoS_2 does not comprise locally transformed phases and atomically sharp interfaces to lower the contact resistance. See D. Voiry et al., *Nat. Mater.* 15, 1003 (2016); and D. Voiry et al., *Nano Lett.* 13, 6222 (2013). Even with the much enhanced electrochemically active surface area, the electronic coupling between the substrate and active sites will be sluggish unless selectively forming the electrically addressable interfaces through heterogeneous doping. Alternatively, both experimental demonstration and theoretical prediction have confirmed that regions of atomically localized curvature lead

to a loss of spatial overlap of the d orbitals with neighboring Mo atoms and a shift in hybridization of Mo—S bonding from mixed ionic-covalent bonding between Mo and S atoms. See L. Yu et al., *Nano Lett.* 16, 2444 (2016); and M. Mavrikakis et al., *Phys. Rev. Lett.* 81, 2819 (1998). Notably, under applied strain, depletion of charges residing on Mo atoms is increased, thus leading to excess charges redistributed around S atoms. The net result of these orbital effects is a drastic increase in energy locally and reduced bonding-antibonding splitting. Consequently, the bandgap decreases, with the valence band maximum (VBM) and conductive band minimum (CBM) crossing the Fermi level, leading to a reduction of overall R_s similar to the semiconductor-to-metal transition and thus improved electronic coupling. See A. P. Nayak et al., *Nat. Commun.* 5, 1 (2014); and H. Li et al., *J. Am. Chem. Soc.* 138, 5123 (2016).

[0033] In parallel, using the measured active sites and exchange current densities, the TOF was calculated to infer the intrinsic catalytic activity per active sites. TOF was determined to be ≈0.130 s^{-1} at −200 mV vs. RHE for 2H c-MoS_2 synthesized at 250° C., an order of magnitude higher than the 2H planar counterpart (0.016 s^{-1}). These results suggest that the improvement of the HER performance comes from the combined effects of dimensional transition. First, the 3D porous morphology not only effectively exposes the initially buried active sites on both edges and basal plane but also facilitates effective transport across various interfaces between 2H c-MoS_2, electrolyte and current collecting CC substrate. Second, the high strain load modulates the ΔG_H and tailors the TOF at each active site. Specifically, the TOF achieved is comparable to or better than values measured for strain-vacancy engineered MoS_2, edge sites of MoS_2, vertical MoS_2 flakes, 1T' MoS_2 nanoparticles, and $[Mo_3S_4]^{4+}$ cluster of amorphous MoS_2. See H. Li et al., *Nat. Mater.* 15, 48 (2016); T. F. Jaramillo et al., *Science* 317, 100 (2017); D. Kong et al., *Nano Lett.* 13, 1341 (2013); H. Wang et al., *ACS Nano* 8, 4940 (2014); and T. F. Jaramillo et al., *J. Phys. Chem. C* 112, 17492 (2008). Although not quite as active as the molecular thiomolybdate $[Mo_3S_{13}]^{2-}$, c-MoS_2 has advantages to synergistically tailor both intrinsic and total electrode activities in tandem with readily scalable synthesis, assembly, and processing routes. See J. Kibsgaard et al., *Nat. Chem.* 6, 248 (2014). Meanwhile, the loading of c-MoS_2 was increased in an attempt to further improve the HER metrics through increasing numbers of active sites. However, HER metrics drastically decreased such that the thickest film in fact exhibited the poorest performance. From the comparison of all three specimens of different thicknesses, it is clear that the major limiting factors are the high η_{10} and low current densities. The high resistance may arise from the discontinuous pathways where outer layers of c-MoS_2 are loosely attached to each other, as suggested by EDX mapping. The limited contacts at the top of the films serve as constriction points, thus diminishing electron accessibility and adversely affecting the overall HER performance. This limitation can be potentially mediated by adding conductive adducts, such as graphene, CNTs, or even 1T' ce-MoS_2, to simultaneously minimize charge transport distance and series resistance, while maintaining the accessible surface area.

[0034] Another important aspect for practical implementation of MoS_2-based HER catalyst is the long-term stability under continuous operation and elevated temperatures. A durability study on the c-MoS_2-based electrodes was first carried out by employing continuous LSV cycles at a scan rate of 5 mV s^{-1}. The HER catalytic activity remains almost unchanged in the first 2500 cycles and displays a negligible decay after 5000 cycles. See M. A. Lukowski et al., *J. Am. Chem. Soc.* 135, 10274 (2013); and Y. Yin et al., *J. Am. Chem. Soc.* 138, 7965 (2016). In parallel, the electrochemical stability of the c-MoS_2 catalyst was also evaluated by prolonged electrolysis at constant potentials. In accordance with the durability tests, the current density of c-MoS_2 remained stable in 0.5 m H_2SO_4 for more than 100 h and showed a negligible change after 110 h. The uniformity and crumpled nanostructure of c-MoS_2 was also examined under SEM and TEM after continuous linear potential sweeps, and appeared to be intact after the degradation measurements. In addition, when subjecting to thermal annealing at 300° C. under ambient conditions, unlike the temperature sensitive 1T' counterparts, 2H c-MoS_2, with in situ strain fields propagating on the thermodynamically favored 2H phase, remained catalytically active, revealing an unparalleled operational window up to 300° C. When the thermal annealing temperature was further increased to 350° C., a transition from MoS_2 to MoO_3 was observed as confirmed by XPS spectra. Nevertheless, the unprecedented combination of electrochemical and thermal stabilities not only suggests the preservation of both catalytic activity and structural integrity of c-MoS_2, consistent with the structural robustness of c-MoS_2, but also renders c-MoS_2 more versatile for long-term utilization in energy conversion devices. Meanwhile, the chemically and mechanically robust nature of c-MoS_2 provides flexibility in using chemical and mechanical means to further improve catalytic properties for HER. See Z. W. She et al., *Science* 355, 146 (2017).

[0035] In summary, the invention enables the formation of 3D structurally deformed c-MoS_2 catalysts for electrochemically stable, thermally resistant, and highly efficient HER. The use of electrostatically charged droplets as nanoreactors facilitates colloidal dispersion, fission, and capillarity-induced-self-crumpling of 2D ce-MoS_2, ultimately transforming it into 3D c-MoS_2. As summarized in Table 1, electrochemical characterization indicates that HER electrodes composed of c-MoS_2 catalysts synergistically integrate advantageous features of morphologically, chemically, electronically, and mechanically engineered MoS_2 catalysts. See J. Kibsgaard et al., *Nat. Mater.* 11, 963 (2012); D. Kong et al., *Nano Lett.* 13, 1341 (2013); H. Li et al., *Nat. Mater.* 15, 48 (2016); D. Voiry et al., *Nat. Mater.* 15, 1003 (2016); H. Wang et al., *ACS Nano* 8, 4940 (2014); and Y. Yin et al., *J. Am. Chem. Soc.* 138, 7965 (2016). These include high surface area, efficient transport at interfaces, reduced series resistance, exposed basal plane with increased density of active sites, improved TOF per active site, chemical and mechanical robustness. The invention simultaneously achieves state-of-art metrics while addressing long-term stability under continuous operation as well as exposure to high temperature treatment while using a fully scalable and easy to integrate process. Given the wide variety and availability of chemically exfoliated 2D functional materials, including graphene, transition metal dichalcogenide (TMD), and the emerging MXenes, structurally robust, thermally stable, electronically heterogeneous, and catalytically active, multifunctional hybrid nanocomposites can now be readily, rapidly, and rationally assembled through this template free and scalable nanomanufacturing route. See J. Luo et al., *ACS Nano* 9, 9432 (2015). This enables applications

beyond HER, including electrochemical capacitors, battery, catalysis, reactors and separation, drug delivery, biocompatible scaffolds, sensing and high complexity composites.

[0036] The present invention has been described as method to form crumpled transition metal dichalcogenide sheets. It will be understood that the above description is merely illustrative of the applications of the principles of the present invention, the scope of which is to be determined by the claims viewed in light of the specification. Other variants and modifications of the invention will be apparent to those of skill in the art.

TABLE 1

Summary of HER characteristics of MoS_2 catalysts with various nanostructures, strain S vacancy, edge and 1T' phase engineering. η_{10}, j_0, R_s and R_{ct} stand for overpotentials, exchange current densities, series and charge-transfer resistances, respectively.

	Total electrode properties							Intrinsic properties			
	η_{10} (mV)	Tafel slope (mV/dec)	J_0 ($\mu A/cm^2$)	$R_s + R_{ct}$ (Ω)	Capacitance (mF/cm^2)	Surface area (m^2/g)	Mass loading ($\mu g/cm^2$)	Active sites ($sites/cm^2$)	TOF (s^{-1})	Stability Cycles	Stability Temp
2H c-MoS_2 (300° C.)	−193	66	10.4	R_s = 1.7 R_{ct} = 13	11.0	310.5	13	5.7×10^{17}	0.128	5000	300° C.
2H c-MoS_2 (250° C.)	−191	64	10.4	R_s = 1.5 R_{ct} = 13	11.4	310.8	13	5.8×10^{17}	0.130	5000	300° C.
2H c-MoS_2 (200° C.)	−309	92	5.2	R_s = 17 R_{ct} = 50	2.2	48.6	13	2.0×10^{15}	0.080	2000	300° C.
2H c-MoS_2 (100° C.)	−340	107	4.5	R_s = 29 R_{ct} = 150	1.1	37.2	13	4.7×10^{14}	0.052	1000	N/A
2H planar MoS_2	−364	108	0.7	R_s = 38 R_{ct} = 275	0.091	19.0	15	1.0×10^{14}	0.016	<1000	N/A
*2H porous MoS_2	−218	62	10.5	R_{ct} = 280	8.2	N/A	140	2.3×10^{14}	N/A	1000	N/A
**Vertically aligned 2H MoS_2	−400	105-120	2.2	R_s = 2.3 R_{ct} > 20	N/A	N/A	8.5	5.4×10^{14}	0.013-0.016	1000	N/A
***Double gyroid MoS_2	−206	50	0.69	N/A	4.8	N/A	60	N/A	N/A	N/A	N/A
****Strained 2H-MoS_2	−170	60	50-60	N/A	N/A	N/A	N/A	3.1×10^{14}	0.08-0.31	N/A	N/A
*1T' Porous MoS_2 nanosheets	−153	43	15.8	R_{ct} = 16	63.1	N/A	140	5.8×10^{16}	0.5 (η = 15 3 mV)	1000	N/A
*****1T' MoS_2 nanoparticle	−118	66	50	R_s = 18 R_{ct} > 5	345	N/A	3,400	6.4×10^{18}	0.10	>5000	N/A
******1T' $MoSe_2$	−152	52	N/A	R_{ct} = 16	25.2	N/A	140	N/A	N/A	1000	N/A
*******1T' WS_2	−142	70	N/A	R_{ct} = 5	48	N/A	1000	N/A	N/A	<500	N/A

*Y. Yin et al., *J. Am. Chem. Soc.* 138, 7965 (2016);
**D. S. Kong et al., *Nano Lett.* 13, 1341 (2013);
***J. Kibsgaard et al., *Nat. Mater.* 11, 963 (2012);
****H. Li et al., *Nat. Mater.* 15, 48 (2016);
*****H. Wang et al., *Acs Nano* 8, 4940 (2014);
******Y. Yin et al., *Adv. Mater.* 29, 1700311 (2017);
*******M. a Lukowski et al., *Energy Environ. Sci.* 7, 2608 (2014).

We claim:

1. A method of crumpling transition metal dichalcogenide sheets, comprising:

forming an electrostatically charged liquid droplet comprising a plurality of planar sheets of a transition metal dichalcogenide;

applying a sufficient electric field to the droplet to cause the droplet to rupture into a plurality of fission droplets by an electrohydrodynamic process, wherein each fission droplet comprises at least one planar sheet of the transition metal dichalcogenide; and

evaporating the remaining liquid from the plurality of fission droplets, thereby inducing spontaneous self-crumpling of the at least one planar sheet of the transition metal dichalcogenide in each of the fission droplets.

2. The method of claim **1**, wherein the transition metal comprises molybdenum or tungsten.

3. The method of claim **1**, wherein the chalcogenide comprises sulfur, selenium, or tellurium.

4. The method of claim **1**, wherein the transition metal dichalcogenide comprises molybdenum disulfide.

5. The method of claim **4**, wherein the planar sheets of molybdenum disulfide comprise 2H phase sheets having basal plane defects and whereby the self-crumpling activates the basal plane defects.

6. The method of claim **1**, wherein the planar sheets of the transition metal dichalcogenide comprise exfoliated sheets.

7. The method of claim **1**, wherein the forming an electrostatically charged liquid droplet comprises feeding a solution of the planar sheets of the transition metal dichalcogenide through a spinneret.

8. The method of claim **1**, wherein the sufficient electric field is greater than approximately 1.25 kV/cm.

9. The method of claim **1**, wherein the evaporating comprises depositing the plurality of fission droplets on a substrate above a deposition temperature.

10. The method of claim **9**, wherein the substrate comprises a hydrogen evolution reaction substrate.

11. The method of claim **9**, wherein the substrate comprises carbon or silicon.

12. The method of claim **9**, wherein the deposition temperature is greater than 200° C.

13. The method of claim **9**, wherein the deposition temperature is greater than 250° C.

14. A method for electrochemical hydrogen evolution, comprising exposing an aqueous electrolyte to a crumpled transition metal dichalcogenide in an electrochemical cell at a sufficient cell voltage to catalyze the electrolysis of water and evolve hydrogen.

* * * * *